MAGNETOHYDRODYNAMICS Vol. 59 (2023), No. 3-4, pp. 335–346
DOI: 10.22364/mhd.59.3-4.6

MHD EFFECTS OF THE ALUMINA DISSOLUTION IN ALUMINIUM ELECTROLYSIS CELLS

V. Bojarevics

University of Greenwich, UK

The numerical modelling of high amperage aluminium electrolysis cells requires to account for a variety of their individual features: electric current and associated magnetic field distribution, ferromagnetic parts effect, the velocity field in the two overlying fluid layers, their interface deformation and wave motion, referred to as MHD instability. The normal electrolytic process is regularly disrupted due to the anode changes and the feeding of alumina (Al_2O_3) particulate material ensuring the continuity of the electrolytic aluminium production. The proposed modelling technique of alumina dissolution uses Lagrangian tracking for feed material particles of different sizes accounting for their inertia, drag in the turbulent flow, the electrolyte layer shape and the electromagnetic force at the location. The feed material initially forms rafts of frozen electrolyte + alumina, which gradually disperse and dissolve depending on the local flow, turbulent diffusion, and the instantaneous concentration level below saturation until reaching a quasi-steady concentration distribution. The concentration of solution is continuously depleted due to the electrolytic metal production. Modelling is applied to illustrate optimization of the commercial cell performance, while avoiding regions of low concentration responsible for increased fluoride gas release due to the low voltage anode effect.
Keywords : aluminium electrolysis cell, alumina dissolution, particle tracking, magneto-hydrodynamics, turbulent mixing.

Introduction. Numerical modelling has become a primary tool for design and optimization of commercial high amperage aluminium electrolysis cells. The design of industrial cells requires to consider a variety of their individual features, such as the electric current and the associated magnetic field distribution, ferromagnetic parts effect, the velocity field in the two overlying fluid layers, and their interface deformation and wave motion, often referred to as MHD instability. The concentration of dissolved alumina (aluminium oxide) in the molten electrolyte needs to be maintained within certain limits to avoid loss of production capacity and to avoid anode effect development when the local concentration drops significantly below the 2% level [1]. The anode effects are normally attributed to a depleted alumina content in the cell, however, there are indications that local high alumina concentration spots at the anode bottom are contributing to the so-called low voltage anode effect due to the carbon wetting variation [1, 2]. The complex physical processes occurring during the alumina powder feeding into the cryolite melt are analysed in [3, 4], where experiments and models are presented to treat the practical alumina powder feeding. In summary, the most important effects are the particle agglomeration, frozen bath formation on the feed material surface, followed by remelting and cluster breakup during the initial few seconds of the powder contact with the molten electrolyte. After the initial few seconds stage, the next longer stage involves the alumina powder particle transport, while each individual particle dissolution rate depends on the convective mixing due to the bubble generated flow and electromagnetic stirring. The important empirical dissolution rates were derived using measurements in the controlled laboratory experiments [3]. These experiments showed that the time required to fully dissolve a batch of typical alumina particles of the sizes between 60–90 μm took about 300 to 600 seconds in the presence of stirring. The experimentally determined dissolution rate, which is controlled by the heat transfer and diffusion, was summarized in

the empirical relation containing an empirical constant approximately valid within the concentration range of practical interest [3].

The alumina mixing over the whole volume of the cryolite bath is mostly determined by the electromagnetic stirring efficiency in the liquid electrolyte layer and by the local turbulence generated by the bubble escape [5–9]. There are many publications devoted to the alumina feeding problem involving different types of mathematical approaches (see, for example, [4–13 and references therein). However, the practical usability of the complex mathematical setup and reliance on the expensive computer resources (commercial codes, long computation times, proprietary codes) prove to be precluding a widespread acceptance of the models. In this communication we aim to develop a software extension (or add-on) to treat the alumina feeding and dissolution, which is a part of the specialised aluminium cell modelling package [16] validated with several commercial potlines (see, e.g., [14, 15] and the included references).

This software is based on the full MHD model of the electrolysis cell using the specialised inputs suitable for fast implementation for a specific cell type [16]. The software computes time-dependent currents, voltages, magnetic fields, bath-metal interface shape and the turbulent magnetically driven flow in the bath and in liquid metal. As an example, Fig. 1*a* shows a representative potline model of the cells as an example. The multiple conductors of the complete electrical supply circuit in the figure are coloured by their computed currents depending on the temperature-dependent resistivity of the bus bars according to the Joule heating, heat transfer to the neighbour bars and losses into the air. The electric current in the individual anodes (as a part of the circuit) is computed continuously, following the time-dependent metal-electrolyte interface variation. The magnetic field of the currents in the complete bus bar network and in the liquid layers is considerably affected by the ferromagnetic steel elements of the cell construction (see the computed magnetic field in the highly non-linear magnetized steel elements shown in Fig. 1*b*).

The dome-shaped time average deformation of the metal surface (Fig. 2) is projected onto the bottom of the whole anode block to account for the anode bottom gradual burnout effect maintaining a constant anode-cathode distance (ACD), which results in the anode shape adjustment [14]. The electric current and the magnetic field distribution in the liquid zone is computed from the whole bus bar network connected to the anodes and cathode collectors, coupled with the cell interior details like the ledge profile, bottom shape, collector connections, electrolyte channels, and the electrochemical voltage drop.

1. Mathematical models.

The present investigation focuses on the fluid flow effect on the alumina concentration following the feeding at user prescribed locations, the feed mass and timing. The composition of the feed material depends on the size distribution of particles and their specific density. The addition of particles of different sizes is treated by Lagrangian methods following the tracks of inertial particles subject to the drag in the turbulent fluctuating electrolyte flow [16]. The global mixing of the electrolyte layer occurs due to the large scale MHD circulation, whereas the gas dynamic flow is treated as the background turbulence generated at the anode edges to contribute to the integral effective turbulent diffusivity. Each moving particle is permitted to gradually dissolve, reduce in size and to contribute as a source to the local concentration field. The basic electrochemical reaction of the aluminium metal production is treated as the negative source contribution in the alumina concentration equation. The variable in time and space source is used to model the concentration field development on the Eulerian grid over long time intervals relevant

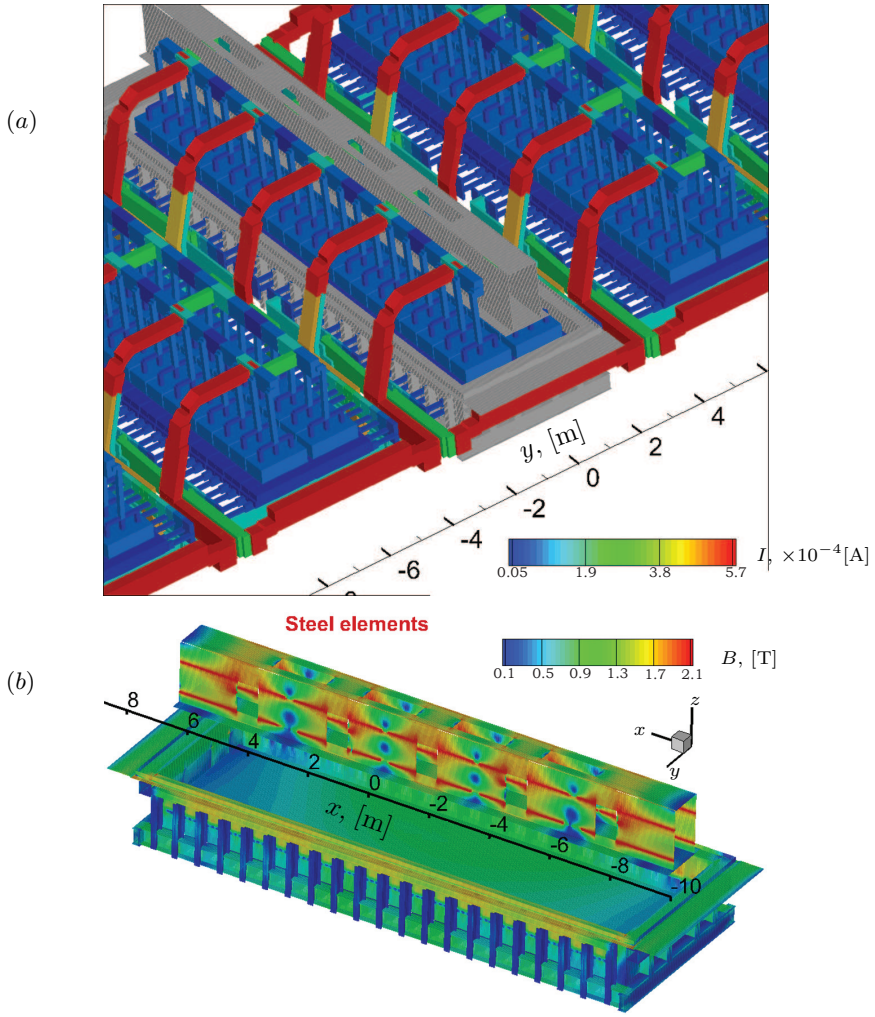

Fig. 1. (*a*) The software MHD-VALDIS generated busbar model for a typical commercial aluminium reduction cell showing the electric current I [A]) distribution in the busbar network. (*b*) The computed magnetic field B [T] in the magnetized steel elements of the cell [14].

to the practical commercial cell operation practices.

The mathematical modelling of this complex time-dependent problem includes the fluid flow solved using the Reynolds averaged and depth averaged turbulent flow model [17–19] for an incompressible fluid with the effective viscosity ν_{e} and turbulent diffusivity α_{e} modified concentration C equation:

$$\partial_t C + \mathbf{v} \cdot \nabla C = \nabla \cdot (\alpha_{\mathrm{e}} \nabla C) + S - P. \tag{1}$$

The concentration $C(x, y, t)$ is treated as the depth averaged quantity due to the small depth of the electrolyte if compared to its horizontal extent (typically, the ratio is approximately $0.05/4 - 20 = 0.0125 - 0.0025$). The turbulent depth averaged flow field with the addition of pulsating part is represented by the velocity $\mathbf{v}(x, y, t)$. The source

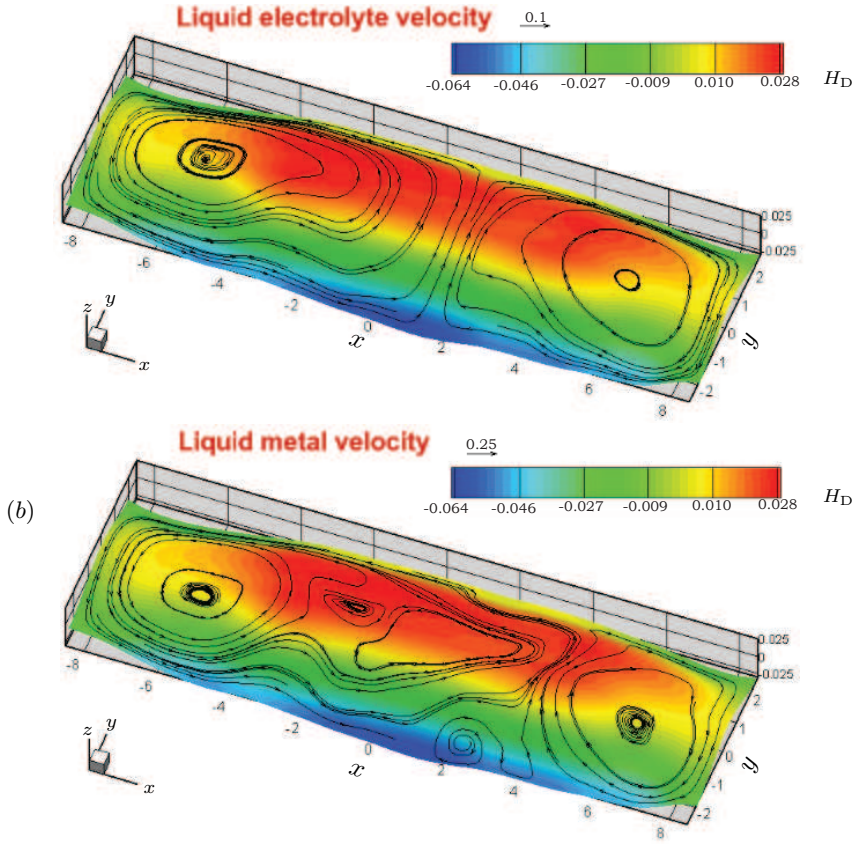

Fig. 2. The dome-shaped electrolyte/liquid metal interface $z(x,y) - z\text{average} = H_D(x,y)$: (*a*) the electrolyte velocity field; (*b*) the liquid metal velocity streamlines in a 500 kA cell.

$S(x,y,t)$ is computed from the dynamic distribution of the dissolving alumina particles of different sizes by the separate particle tracking solution at the given time moment over the full extent of the electrolyte layer:

$$S = k_2(C_{\text{sat}} - C)\frac{A}{\mathrm{d}V}N_{\text{sc}}, \tag{2}$$

where $k_2 = 1.0{\cdot}10^{-6}$ (m/s) is the empirical dissolution rate constant from [2, 3], $C_{\text{sat}} = 164.6$ (kg/m^3) ($\approx 8\%$) is the saturation level of the alumina in the cryolite melt, $A(x,y,t)$ is the total surface area of all particles in the local computational grid element of volume $\mathrm{d}V$, and the number N_{sc} is the scaling factor introduced to represent the correlation from the total number of particles used in the numerical simulation ($\sim 10^4$) and the actual mass of the alumina fed to the liquid bath. The alumina concentration loss $P(x,y,t)$ is determined by the Faraday law (the electrochemical reaction of aluminium metal reduction from the alumina in the melt):

$$P = k_{\text{e}} j \frac{1.93}{h_{\text{el}}}, \tag{3}$$

where $k_{\text{e}} = 9.33{\cdot}10^{-8}$ [kg/(A·s)] is the electrochemical equivalent for the aluminium metal,

j (A/m^2) is the local electric current density, h_{el} is the electrolyte depth, and the coefficient 1.93 relates to the amount of alumina used to produce the aluminium metal.

The effective diffusivity α_{e} in Eq. (1) is defined as the sum of laminar α and turbulent diffusivity α_{T} related to the turbulent mixing and determined by the turbulent viscosity ν_{T}:

$$\alpha_{\mathrm{e}} = \alpha + \alpha_{\mathrm{T}} = \alpha + \mathrm{Sct}\nu_{\mathrm{T}}, \quad \nu_{\mathrm{e}}(x,y,t) = \nu + \nu_{\mathrm{T}}(k,\omega). \tag{4}$$

The simplest model for Sct is the Reynolds analogy, which yields a turbulent Schmidt number of $\mathrm{Sct}=1$. The ν_{T} distribution is obtained by solving the time dependent k-ω two-equation model [17, 18]. The k-ω model is a variant of low Reynolds number turbulence models which permits to resolve the flow from laminar to the fully developed turbulent state. The ω variable is related to the reciprocal turbulent time scale (frequency of vorticity fluctuations) and the k variable is the turbulence kinetic energy. The depth averaging in the shallow layer approximation adds new terms in the model permitting to account for the damping in a variable depth layer and the additional turbulence generation at the edges of the anodes due to the bubble flow.

To determine the surface area of all particles in the local computational element $A(x,y,t)$ in Eq. (2), the dynamic Lagrangian particle tracking algorithm was implemented. The position $\mathbf{R}(x,y,z,t)$ of an individual particle can be determined following its path in the liquid electrolyte volume according to the variable total force $\mathbf{F}(x,y,z,t)$ acting on each particle at a given time moment [19, 20]:

$$\partial_t \mathbf{R} = \mathbf{u}_{\mathrm{p}}, \quad m_{\mathrm{p}}\partial_t \mathbf{u}_{\mathrm{p}} = \mathbf{F}, \tag{5}$$

where $\mathbf{u}_{\mathrm{p}}$ is the particle's velocity and m_{p} its mass. The force $\mathbf{F}$ acting locally on a spherical particle can be decomposed into the fluid drag force $\mathbf{F}_{\mathrm{d}}$, the buoyancy force $\mathbf{F}_{\mathrm{g}}$ and the effective electromagnetic (EM) force $\mathbf{F}_{\mathrm{e}}$. The drag force depends on the particle Reynolds number

$$\mathrm{Re}_{\mathrm{p}} = r_{\mathrm{p}}|\Delta\mathbf{u}|/\nu, \tag{6}$$

where r_{p} is the particle's radius, $\Delta\mathbf{u} = \mathbf{u} - \mathbf{u}_{\mathrm{p}}$ is the (slip) velocity relative to the fluid velocity $\mathbf{u}$, ν stands for the kinematic viscosity. For small particles ($1-100\,\mu$m) the Reynolds number Re_{p} is rather small of the order of $0.1-10$, therefore, the drag force can be approximated as an instantaneous modified Stokes formula [20]. The buoyancy force due to the gravity $\mathbf{g}$ action on the particle and surrounding fluid is projected along the dome-shaped electrolyte layer top $z = H_2(x,y)$:

$$\mathbf{F}_{\mathrm{g}} = (\rho_{\mathrm{p}} - \rho)V_{\mathrm{p}}\mathbf{g}\cdot\mathbf{e}_z\frac{\nabla H_2}{|\nabla H_2|}, \tag{7}$$

with ρ being the fluid density, ρ_{p} the particle density, V_{p} the particle volume.

In principle, the electromagnetic force acts directly on the electric current if it passes through the particle, however, the EM force distribution in the surrounding fluid leads to an additional pressure redistribution on the surface of the particle, which results in an additional total force on the particle [22, 23]. For the case of electrically non-conducting particles (alumina, carbon dust, bubbles, etc.), the effective EM force (from the pressure redistribution) acts on the particles embedded in the fluid. The effective resultant force $\mathbf{F}_{\mathrm{e}}$ on the particle can be represented by the EM force in the fluid $\mathbf{f}_{\mathrm{e}}$ at the location of the particle [22]:

$$\mathbf{F}_{\mathrm{e}} = -V_{\mathrm{p}}\frac{3}{2}\mathbf{f}_{\mathrm{e}}, \tag{8}$$

Note, that Leenov and Kolin [22] derived a similar expression for uniform magnetic and electric fields

$$\mathbf{F}_{\mathrm{eDC}} = -V_{\mathrm{p}}\frac{3}{4}\mathbf{f}_{\mathrm{e}}, \tag{9}$$

which gives a two times smaller force acting on a non-conducting particle, however, Eq. (8) was derived for a non-uniform magnetic field distribution like the field in the electrolysis cell. The drag expression for a spherical particle needs some modification due to the acceleration or deceleration in the turbulent flow [20,24] as

$$\mathbf{F}_{\mathrm{d}} = 6\pi\nu\rho r_{\mathrm{p}}\left[\Delta\mathbf{u} + \frac{r_{\mathrm{p}}^2}{9\nu}\frac{\mathrm{d}\Delta\mathbf{u}}{\mathrm{d}t}\right], \tag{10}$$

where Eq. (10) contains the instantaneous Stokes drag, the memory term (Basset force) and the added mass force.

The typical mixing flow in the electrolyte is turbulent ($\mathrm{Re} \sim 10^3 - 10^4$), which further requires a modification due to the stochastic part of fluid velocity in accordance with the resolved turbulent kinetic energy k and local eddy lifetime (or the particle transit time in that eddy, whichever is the shortest) [20]. The use of the k-ω turbulence model in the code facilitates obtaining these quantities, which are locally interpolated to the particle position at each time step. The numerical integration of Eqs. (5) is done for each individual particle of various properties depending on the initial seeding locations. The time dependent forces $\mathbf{F}(x, y, t)$ are sensitive to the location and instantaneous update of the local slip velocity $\Delta\mathbf{u}$ (including the stochastic contribution). The numerical scheme proposed in [25] permits a stable time integration of the particle tracks with the time steps of the order of $0.01 - 0.1$ s used for the unsteady concentration solution of Eq. (1) in the examples presented below.

2. Examples of numerical results.

A representative test cell of 500 kA total current was used in this study to illustrate the alumina particle transport and dissolution in the liquid cryolitic bath. The software gives the user a choice for feeder locations and feeding repeat time intervals. The option to add up to sixteen feeders is currently implemented. Each feeder can be set to supply a different mass of alumina powder. The choice of representative particle sizes permits three different particle sizes which will be equally distributed in the feed material. The initial concentration of the alumina is assumed to be constant, prescribed by the user. In the following examples a 2% concentration is used, corresponding to 41.5 kg/m^3 in the physical units.

After feeding the particles they are subject to a turbulent flow field including the stochastic fluctuating part. The turbulent diffusion spreads the concentration according to the local concentration in the position of each particle. Initially, the local batch of particles is surrounded immediately by a high concentration near field which slows down the dissolution according to Eq. (2). Fig. 3 shows the sequence of the particle cloud and raft motion, followed by the dissolution adding to the concentration field in the volume of the bath. The first frame shows the clusters after 10 s of the first feeding cycle when these are slowly starting to move with the flow. The feeder positions are indicated by the large black circles, the large pink dots show rafts, and the variable size and color dots correspond to particles (initially in clusters). Feeder N3 is in the middle position, where the flow is weak, therefore, the particle cluster moves slowly. The flow and turbulent diffusion help to spread the particles and the concentration, as seen from

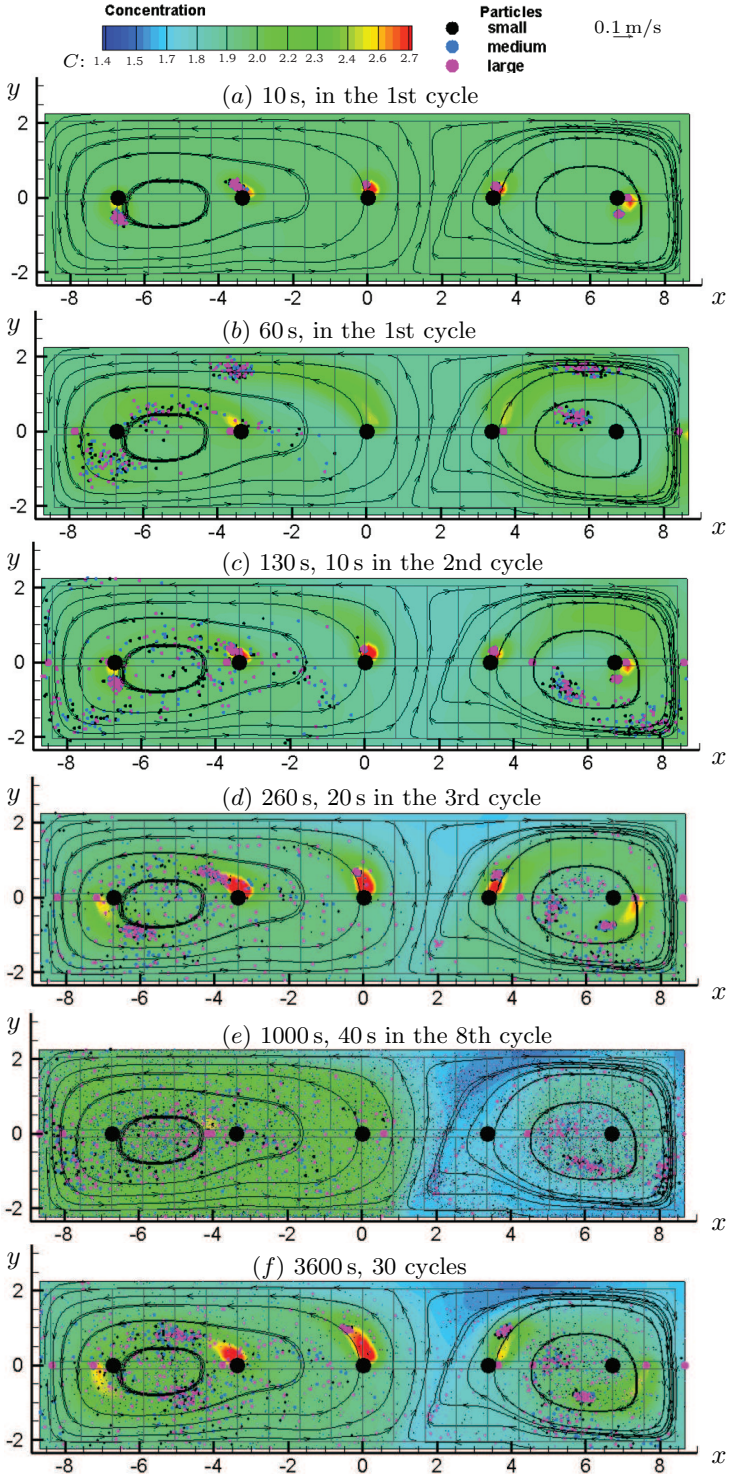

Fig. 3. Particles and concentration during normal feeding stages. The black circles indicate the location of five feeders each supplying 2.17 kg of alumina at 120 s intervals.

the second frame at 60 s. The feed mass and the feeding intervals are prescribed in the software input individually for each feeder. In this example we used an equal mass of 2.17 kg supplied to each feeder at regular intervals of 120 s. When at 120 s the second batch of the feeding material is added, the third frame shows the distribution of the particles and the concentration at 130 s. The fourth frame shows the particles added at the third cycle and the previously added and partly dissolved particles contributing to the concentration field distribution. After a long run of 1000 s the particle and the concentration distribution are shown in the fifth frame (Fig. 3*e*). Eventually, the sixth frame shows the particles and the established concentration after 1 hour of mixing (30 cycles of feeding, Fig. 3*f*). The sizes of the particles in the images are dynamically adjusted as these gradually dissolve, becoming smaller in diameter. The small particles of 50 μm diameter (black dots) are disappearing very fast as they shrunk in size, the medium size 75 μm particles (blue) stay visible for a couple of cycles, while the large ones of 100 μm size (pink) continue to travel for a considerable time length of 300 – 600 s, which confirms the experimental dissolution rates observed in [2, 3, 7]. The regions of high overfeed and underfeed are clearly visible in Fig. 3*f*, however, the time-dependent nature of the feed pattern means that the last feed clusters of the particles are still travelling in the fluid for some time. The effects of the alumina loss P given by Eq. (3) due to the aluminium metal reduction led to the regions of very low concentration clearly visible in Fig. 3*f* after the 3600 s development in this case.

The overall balance of the feeding process is illustrated by numerically computed data collected in Table 1. The initial 2% concentration is approximately conserved after 1 hour feeding and metal production in the electrolytic process. The solution is obtained in 18 minutes of the PC run time using time steps of 0.1 s to solve numerically the mathematical problem (1)–(8) using the velocity and turbulence properties computed before. This permits a rather quick and flexible method to optimize the feeding process for a commercial cell.

The effects of the initial raft formation are illustrated in Fig. 4*a*. The oscillations of the average concentration correspond to the feeding cycles of 120 s. If the rafts are ignored in the model (black dashed line), the concentration drops to a lower level due to the faster dissolution and electrochemical consumption. The high raft percentage resulting from the initial feed (solid blue line) produces a higher average concentration, although the difference is not very large at 0.1%.

In commercial practice the feeding follows a variation in the feed amount by overfeeding or underfeeding the cells for certain time intervals. This helps to identify the problems in cell operation. Fig. 4*b* illustrates the variation of the average concentration computed for the regimes of optimal feeding (2.17 kg per feeder), overfeeding (2.387 kg) and underfeeding (1.953 kg).

Table 1. Summary after 1 hour feeding.

Initial uniform concentration 2% (41.5 kg/m^3)	129.24 kg
In 3600 s feeding 2.17 kg each feeder at 120 s intervals	325.5 kg
In 3600 s spent to metal production	324.8 kg
After 3600 s left in solution	127.22 kg
in particles	5.83 kg
Average concentration	1.97%
Accumulated error	–0.68%

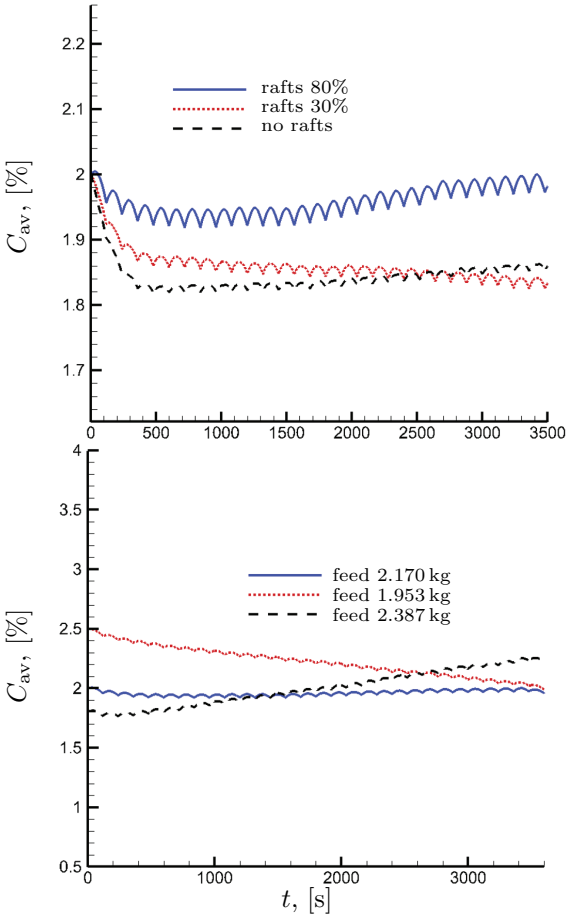

Fig. 4. Average concentration variation during the 1 hour feeding period: (*a*) the effect of the initial rafts/particle's ratio, (*b*) normal feeding (2.17 kg per cycle) compared to overfeeding (2.387 kg) and underfeeding (1.953 kg).

Another feeding variation is required when in the production cell an anode reaches its lifetime and needs a replacement. Typically, 1 or 2 anodes from the total number of 20 to 50 need to be replaced in a day. When a new anode is installed, it's temperature is lower than the surrounding cryolite bath, leading to a frozen bath layer and partially restricting the electric current passage. The software permits users to investigate this scenario and how this affects the alumina feeding. Fig. 5*a* shows the significant concentration disturbance if the normal feeding (2.17 kg per feeder) is maintained during a particular anode N30 replacement and the modification of the velocity field. A simple modification of the feeding distribution over the individual feeder tubes leads to a restored nearly uniform concentration during this critical period.

Conclusions.

The combination of the Lagrange and Eulerian treatment of the alumina feed to the cryolite melt permits a realistic simulation and optimization of the alumina feeding using a combination of flexible options controlled by the software user. The predicted distributions confirm the general experimental observations of a rather slow dissolution process. The particle size is particularly important to achieve the desired uniform spread

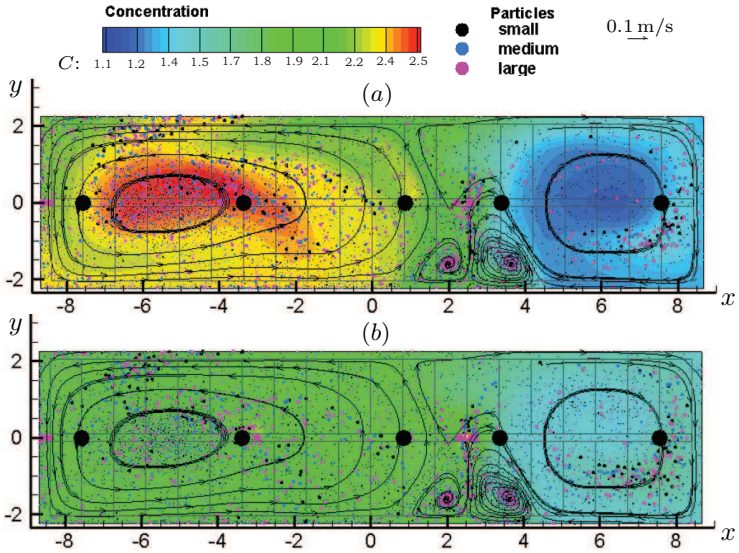

Fig. 5. The case of the perturbed velocity field due to anode N 30 change. Effect of the variable feed amount to different feeders after 1 hour concentration variation during the one hour feeding period, average concentration is 2%: (*a*) highly nonuniform concentration distribution if using the normal amount of alumina (2.17 kg) to all feeders, (*b*) optimized feeder loads: 2 kg to feeders N1-N4, and 2.5 kg to feeder N5 at each cycle of 120 seconds.

of concentration. Regions of high or low local concentration can develop in the bath below anodes, which could significantly decrease the cell's efficiency. The obvious next steps will be the industrial comparisons for the concentration distribution with accurate and reliable tests on commercial cells.

References

[1] J. Thonstad, T.A. Utigard, H. Vogt. *On the anode effect in aluminum electrolysis* (Eds. G. Bearne, M. Dupuis, G. Tarcy, Essential Readings in Light Metals. Springer, Cham, 2016), pp. 131–138.

[2] T.A. Aarhaug, A.P. Ratvik. Aluminium primary production off-gas composition and emissions: An overview. *JOM*, vol. 71 (2019), no. 9, pp. 2966–2977.

[3] R.G. Haverkamp, B.J. Welch. Modelling the dissolution of alumina powder in cryolite. *Chem. Eng. Processing*, vol. 37 (1998), pp. 177–187.

[4] A. Solheim. *A novel design criterion for alumina feeders in aluminium electrolysis cells* (Ed. J. Grandfield, Light Metals, 2014, TMS), pp. 711–716.

[5] R. von Kaenel, J. Antille, M.V. Romerio, O. Besson. *Impact of magnetohydrodynamic and bubble driving forces on the alumina concentration in the bath of Hall–Héroult cell* (Ed. B Sadler, Light Metals, 2013, TMS), pp. 585–590.

[6] H. Zhang,S. Yang, H. Zhang, J. Li, Y. Xu. Numerical simulation of alumina mixing process with a multicomponent flow model coupled with electromagnetic forces in aluminum reduction cells. *JOM*, vol. 66, (2014), no. 7, pp. 1210–1217.

[7] B. Bardet, T. Foetisch, S. Renaudier *et al.* *Alumina dissolution modelling in aluminium electrolysis cell considering MHD driven convection and thermal impact* (Ed. E. Williams, Light Metals, 2016, TMS), pp. 315–319).

[8] K.E. Einarsrud, S.E. Gylver, E. Manger. *CFD modelling of alumina feeding* (Ed. O. Martin, Light Metals, 2018, TMS), pp. 557–564).

[9] D.S. Severo, V. Gusberti, P. Navarro and P. Domnguez. Numerical modeling of the alumina distribution in aluar cells. Travaux 47. In: *Proc. the 36th International ICSOBA Conference, Belem, Brazil, 2018*, pp. 931–946.

[10] Xiaozhen Liu, Youjian Yang, Zhaowen Wang *et al.* CFD modeling of alumina sdffusion and distribution in aluminum smelting cells. *JOM*, vol. 71 (2019), no. 2, pp. 764–771.

[11] T.C.W. Lau, J.H. Frank and G.J. Nathan. Resolving the three–dimensional structure of particles that are aerodynamically clustered by a turbulent flow. *Phys. Fluids*, vol. 31, (2019), 071702, pp. 1–5.

[12] J.P. Kissane. *Optimising Alumina Feeders in Aluminium smelting pots* (PhD Thesis, University of Wollongong, Australia, 1995).

[13] P. Lavoie, M.P. Taylor, J.B. Metson. A review of alumina feeding and dissolution factors in aluminium reduction cells. *Metall. Materials Trans.*, vol. 47B (2016), pp. 2690–2696.

[14] V. Bojarevics, E. Radionov, Y. Tretiyakov. *Anode bottom burnout shape and velocity field investigation in a high amperage electrolysis cell* (Ed. O. Martin, Light Metals, 2018, TMS), pp. 551–556.

[15] V. Bojarevics and J.W. Evans. Mathematical modelling of Hall–Héroult pot instability and verification by measurements of anode current distribution. *TMS, Light Metals*, 2015, pp. 783–788.

[16] V. Bojarevics. *MHD–VALDIS Reference Manual* (University of Greenwich, 2023), 78 p.
https://www.dropbox.com/scl/fi/6rzsbw12z7ckopx73407v/MHD_VALDIS_Manual_2023.pdf?rlkey=3o4ut4qwikmvppev75l1f2r8u&dl=0.

[17] V. Bojarevics. In-line cell position and anode change effects on the alumina dissolution. *TMS Light Metals*, 2021, pp. 584–590.

[18] D.C. Wilcox. *Turbulence Modelling for CFD* (2nd ed., DCW Industries, California, 1998), 522 p.

[19] A.K. Rastogi, W. Rodi. Prediction of heat and mass transfer in open channels. *J. Hydraulics Division ASCE*, HY3 (1978), pp. 397–420.

[20] P.G. Tucker. Computation of particle and scalar transport for complex geometry turbulent flows. *J. Fluids Eng.*, vol. 123 (2001), pp. 372–381.

[21] R. Clift, J.R. Grace, M.E. Weber. *Bubbles, Drops, and Particles* (Dover Publications, New York, 2005), 381 p.

[22] V. Bojarevics, J. Freibergs, E. Shilova, E. Shcherbinin. *Electrically Induced Vortical Flows* (Chapter 6, Kluwer Academic Publishers, Dordrecht, Boston, London, 1989), 379 p.

[23] D. Leenov, A. Kolin. Theory of electromagnetophoresis. *J. Chem. Phys.*, vol. 22 (1954) 4, pp. 683–688.

[24] L.D. Landau, E.M. Lifshitz. *Fluid Mechanics* (Pergamon Press, 1987), 532 p.

[25] V. Bojarevics, K. Pericleous, R. Brooks. Dynamic model for metal cleanness evaluation by melting in cold crucible. *Metall. Materials Trans.*, vol. 40B (2009), pp. 328–336.

Received 24.11.2023